Available online at www.sciencedirect.com

ScienceDirect

journal homepage: http://www.elsevier.com/locate/acme

Original Research Article

Investigations on mechanical properties and microtopography of electromagnetic self-piercing riveted joints with carbon fiber reinforced plastics/aluminum alloy 5052

Jusong Liang [a], *Hao Jiang* [a], *Jinsheng Zhang* [b], *Xianhe Wu* [b], *Xu Zhang* [c], *Guangyao Li* [a], *Junjia Cui* [a,*]

[a] *State Key Laboratory of Advanced Design and Manufacturing for Vehicle Body, Hunan University, Changsha 410082, China*

[b] *Chongqing Changan Automobile Co. Ltd, Chongqing 401120, China*

[c] *College of Automotive and Mechanical Engineering, Changsha University of Science and Technology, Changsha 410114, China*

ARTICLE INFO

Article history:
Received 23 June 2018
Accepted 2 November 2018
Available online 21 November 2018

Keywords:
Electromagnetic self-piecing riveting
Mechanical properties
Microtopography
Carbon fiber reinforced plastics

ABSTRACT

In this paper, the mechanical properties of electromagnetic self-piercing riveted (E-SPR) joints with carbon fiber reinforced plastics (CFRP)/aluminum alloy (Al) 5052 were comprehensively investigated. Microtopography observations, hardness measurements and tensile-shear strength tests were performed by comparing with regular pressure self-piercing riveted (P-SPR) joints. Results showed that the undercut value of E-SPR joints was higher than that of P-SPR joints. The hardness values on rivet legs of E-SPR joints were larger and almost no difference on rivet heads between the E-SPR and P-SPR. In addition, it was found that mechanical properties of E-SPR joints were higher than that of P-SPR joints. The shear fracture appearance indicated that E-SPR joints with higher undercut were more difficult to rupture in the bottom of Al sheet.

1. Introduction

Using lightweight materials is an effective technology to reduce the mass of automobiles, thereby reducing emissions and saving fuel consumption [1]. Hybrid designs which combine dissimilar materials, such as composites and metals are considered as a cost-effective approach [2]. Comparing with aluminum alloys, carbon fiber reinforced plastics (CFRP) are considered to be an alternative to steels due to its advantages, such as stiffness- and strength-to-density [3]. In addition, the application of CFRP in vehicle body can save up to 10% and 50% in weight compared with aluminum and steel structure, respectively [4].

* *Corresponding author.*
E-mail address: cuijunjia@hnu.edu.cn (J. Cui).

https://doi.org/10.1016/j.acme.2018.11.001

Self-piercing riveting (SPR) has been demonstrated to be a high-efficiency mechanical fastening process in joining dissimilar materials [5]. Comparing with conventional riveting and bolting, SPR process does not require pre-drilled holes, which could reduce production costs and time [6]. Comparing with regular welding technique, SPR could solve the issue of metal and non-metal connection [7]. Moreover, SPR joints between aluminum to aluminum, aluminum to steel and magnesium to magnesium also have better static strength and superior fatigue behavior compared to resistance spot welding (RSW) [8–10]. Therefore, SPR technique has been widely applied in automotive structural [11,12]. Moreover, the space industries and marine have widely used of lightweight materials, even more CFRP and aluminum alloy joined by SPR [13]. And a higher tensile capacity makes the SPR joints have better application in the civil engineering industries [14].

At present, most numerical and experimental studies focused on the effect of process parameters on mechanical properties of SPR joints [15–19]. Especially there were many studies investigated the mechanical properties of SPR joint between metals, such as aluminum to steel [20], aluminum to copper [21] and steel to steel [22]. Zhang et al. [20] found that the thickness and strength of sheets had significantly effect on mechanical and fatigue performance of SPR joints. He et al. [21] demonstrated that both static and fatigue strength of SPR joints increased when enhanced the stiffness of joints. Haque et al. [22] investigated the mechanical behavior of SPR joints between steel sheets in the loading condition of lap-shear and cross-tension. They found that the thickness and hardness of sheet materials and die depth had significantly influenced on the strength of joints. Note that aforementioned studies mainly focused on the strength of SPR joints which could be enhanced by optimizing the strength and structures of sheets.

In addition, many researchers investigated the influence of riveting velocity on mechanical performances of the joints [23–25]. These results showed that the riveting velocity could improve the joint performance. Hahn et al. [23] investigated the shear strength of SPR joints of aluminum alloy sheets using the drop hammer which the impact velocity could be over 100 m/s. Results showed that the mechanical properties were better than that of conventional SPR joints (riveting velocity of 0.01 m/s). Wang et al. [24] proposed a new SPR process using a gunpowder to drive the riveting process. The mechanical properties and impact performances of SPR joints were investigated and the result showed that the impact SPR joints presented similar or higher shear and fatigue performances compared with conventional SPR and spot-welded joints. Li et al. [25] examined the influence of setting velocity on joint performances. Results showed that the head height of the rivet decreased and the interlock increased when increased the setting velocity, and the static lap shear strength of joints also increased. Above mentioned studies showed a positive effect of high riveting velocities in SPR process. However, drop hammer and gunpowder had a complex process, which were difficult to realize automatic controlling.

Electromagnetic riveting (EMR) is a new joining process based on electromagnetic forming technology [26–29]. Many studies have been carried on EMR technique [30–32]. For instance, Repetto et al. [30] firstly presented a finite element method to analyze the EMR process. Results demonstrated that the EMR obtained a high loading speed in an extremely short period. Cui et al. [31] further established a high-precision electromagnetic-mechanical-thermal coupling model to simulate the EMR process. They found that the riveting velocity for discharge energy of 5 kJ was about 4.8 m/s, and the results were verified by experimental measurements. This paper focused on the forming mechanism of adiabatic shear bands and microstructure evaluation of electromagnetic riveting with different rivet dies by simulation and experiments. Huffer [32] designed a low-voltage handheld electromagnetic riveter, and the maximum impacting velocity could reach 10 m/s. It could be seen that EMR technique had the ability to realize high speed riveting. However, the previous works focused only on the conventional rivets with cup head, not self-piece rivets.

This paper is aimed to investigate the mechanical properties and microtopography of the electromagnetic self-piercing riveting (E-SPR) joints. In addition, regular pressure self-piercing riveting (P-SPR) with a quasi-static speed (2 mm/min) was employed as the comparing process. Firstly, the process parameter studies of E-SPR process were explored in order to obtain the optimal discharge energy. Secondly, microtopography observations and hardness measurements were performed on the cross-section of riveted specimens. Finally, tensile-shear strength was tested and fracture appearances were observed.

2. Materials and methods

2.1. *Specimen preparation*

In this paper, 5052 Al and CFRP sheets were riveted using semi-tubular rivets with flat head, which the material was 35# carbon steel and obtained from Böllhoff (P-SK 5 × 6). All Al sheets were cut along the rolling direction. CFRP sheets were made of AG-80 epoxy and T300 unidirectional fibers fabrics. The resin had 40% volume fraction, and CFRP sheets were obtained by overlaying 17 layers (ply orientation of 0°/90°) with a thickness of 0.15 mm/layer. Chemical compositions and mechanical properties of Al sheets and rivets are presented in Tables 1 and 2, respectively. The mechanical properties of CFRP are shown in Table 3.

Fig. 1(a) shows geometry dimensions of CFRP/Al self-piercing riveted lap joints. The size of CFRP and Al sheets were 140 × 40 × 2.5 mm and 140 × 40 × 2 mm, respectively. The length of overlapping area was 40 mm. Fig. 1(b) shows geometry dimensions of rivets. The geometry dimensions of

Table 1 – Mechanical properties and chemical compositions of 5052 Al sheets [33].

Density (kg/m^3)	Yield strength (MPa)	Tensile strength (MPa)	Si	Fe	Mg	Cr	Al
2680	185.26	234.18	0.25	0.40	2.6	0.20	balance

Table 2 – Mechanical properties and chemical compositions carbon steel rivets.

Density (kg/m^3)	Hardness (HV)	C	Cr	Si	Mn	Cu	P	Fe
7870	750	0.35	0.30	0.30	0.10	0.025	0.025	balance

Table 3 – Mechanical properties of carbon fiber composite sheets.

Fiber density (kg/m^3)	Fiber modulus (GPa)	Fiber strength (MPa)	Tensile strength (MPa)	Tensile modulus (GPa)	Ply thickness (mm)	Resin content (%)
1760	230	3530	911	76	0.15	40

corresponding rivet profiled die which was also obtained from Böllhoff are shown in Fig. 1(c).

2.2. *Riveting methods*

Fig. 2(a) shows the schematic of the E-SPR process. The riveting equipment mainly consists of the electromagnetic setup and riveting mold. The electromagnetic setup is used to provide riveting energies. Firstly, switches on k1 and the electromagnetic setup charges capacitors through direct currents. After the charging process, the electromagnetic setup switches on k2 automatically and the stored electric energies are released through discharging coil. The alternating pulse current with a high amplitude passes through the coil, and a strong electromagnetic field generated around it. The eddy currents were produced in the driving plate (copper) exposed in the electromagnetic field. As the electromagnetic field direction from the coil was opposite to that from the driving plate, the powerful Lorenz repulsion generated and pushed the punch to impact the rivet [34].

It can be seen in Fig. 2(b) that the riveting mold mainly includes a blank holder and die. The blank holder restricts the warp of sheets and guides the rivet. The rivet penetrates the top sheet under the impact of the punch and expands in the die, which forms an interlocking structure within the bottom sheet.

Fig. 2(c) and (d) show the typical cross-section of the riveted joint and partial enlarged detail, respectively. There are three significant structural parameters: the bottom thickness Δt_1, the remaining thickness Δt_2 and the undercut Δt_3 [35]. The bottom thickness represents the axial thickness between rivet leg and the lower surface of bottom sheet. The remaining thickness represents the thinnest thickness from rivet leg to bottom sheet. The undercut represents the horizontal distance from the outer edge of the rivet leg to the lowest edge point of the top sheet. Generally, the remaining thickness should be thick enough to prevent the bottom sheet from fracture.

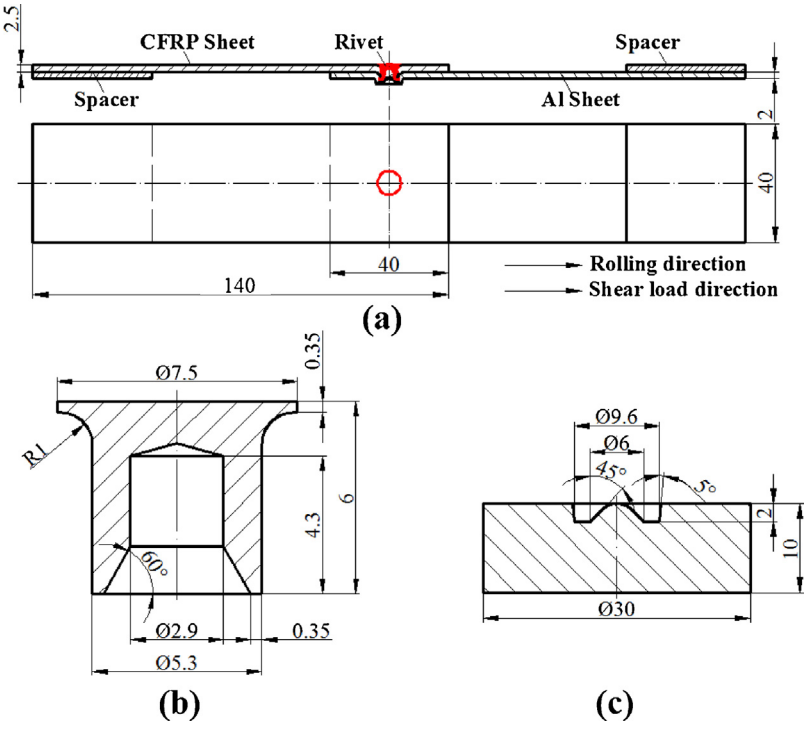

Fig. 1 – Geometry dimensions on the riveted specimen, rivet and rivet die (dimensions in mm): (a) the SPR specimen for tensile-shear tests, (b) the rivet and (c) the die.

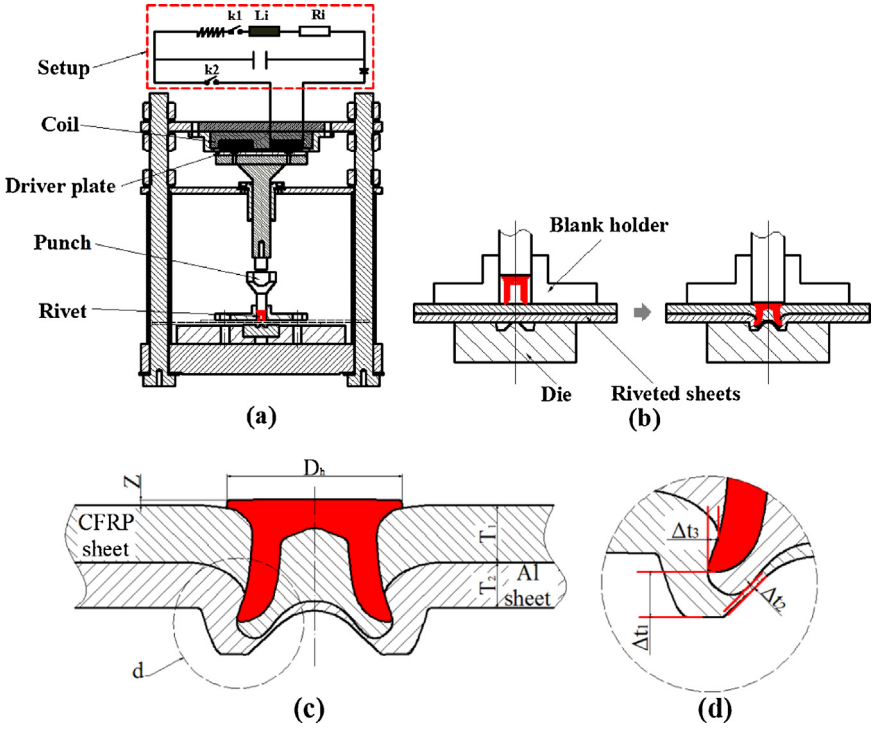

Fig. 2 – The schematic of E-SPR process: (a) equipment, (b) riveting process, (c) evaluation parameters and (d) partial enlarged detail.

Besides a high undercut value demonstrates that the interlocking of the SPR joint is excellent. In addition, another evaluation parameter of the presentation quality is head height (Z), which represents the height difference between rivet head and upper surface of the top sheet.

Fig. 3 shows the E-SPR equipment and high-speed camera. The E-SPR experiments were carried out by a PS 48-16 electromagnetic forming equipment (produced by PST Company). It has a maximum capacitance of 408 μF and a maximum discharge energy of 48 kJ [32]. A measurement method [31] was used to measure the impact velocity by digital image correlation (DIC) camera.

Fig. 4 depicts punch speed-punch displacement curves during E-SPR process. It could be seen that the riveting speed increased rapidly and reached the maximum value (around 7.2 m/s). Subsequently, the riveting speed began to decrease due to the increase of the rivet resistance and the decrement of discharge energy. It could be observed that the whole riveting process was completed in 2 ms. This further demonstrated that the E-SPR process had a high impact velocity.

Fig. 5 depicts the equipment and diagram of P-SPR process. Instron 5985 universal testing machine was used to join P-SPR specimens with a 2 mm/min punch speed. It could be seen that the riveting mold included punch, blank holder, die and pedestal. To ensure that the height of the rivet head was consistent with that of E-SPR joints, the press amount was set to 6 mm.

2.3. *Test methods*

In order to evaluate the riveting quality, SPR joints were split along the axis of rivets and mechanically polished. The Olympus OLS4100-SAF laser con-focal microscope was used to observe microtopography. After that, the cross-section hardness values of rivet after SPR process were measured by Wilson TUKON 1102 Vivtorinox micro-hardness tester at room temperature 25 °C. Ten times objective lens was used for adjusting the height of platform and focusing the cross-section of joints. Pressurized the cross-section of rivet with 1 kg using a rhombus punch and keep pressure for 10 s. And then measure the size of rhombus hole in both horizontal and vertical directions to obtain rivet hardness. Tensile-shear strength tests were performed by Instron 5985 universal testing machine with a quasi-static velocity of 2 mm/min.

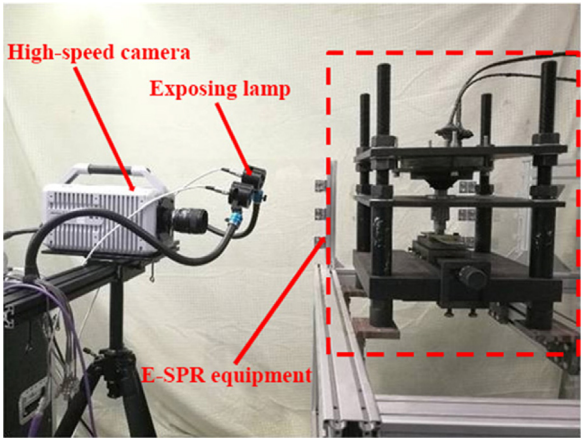

Fig. 3 – The diagram of the EMR equipment and high-speed camera [31].

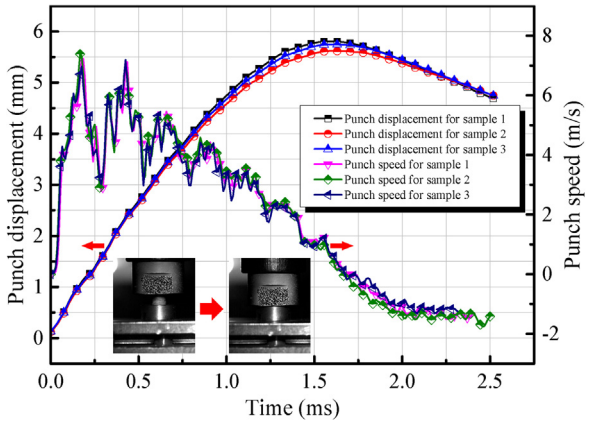

Fig. 4 – The E-SPR process punch speed–punch displacement curves.

Fracture appearances after shear tests were characterized with QUANTA 200 Scanning Electron Microscope.

3. Results and discussion

3.1. *Process parameters analysis*

The discharge energy plays an important role in the formability of riveted joints during the E-SPR. Some exploratory experiments were made and the discharge energy should be in the range of 4.9–5.9 kJ [34,36]. Fig. 6 shows cross-section geometries of E-SPR joints with different discharge energies. The values of head height (Z) and undercut Δt_3 were calculated on the figures. It could be obviously observed that the head height (Z) decreased and the undercut Δt_3 increased with the increase of discharge energy. For the low discharge energy (below 5.3 kJ), the head height exceeded 0.27 mm. The rivet head protruded excessively and the rivet inserted incompletely into the top sheet. The undercut was lower, causing that the Al sheet and rivet leg could not form an interlocking structure. For the high discharge energy (over 5.7 kJ), the CFRP sheet was embedded over 0.56 mm. The CFRP sheet was not only damaged, but the rivet leg and Al sheet had a large deformation.

In addition, the head height was also considered as a quality parameter of SPR joints, and further affected mechanical properties [35]. Three repeated tensile-shear experiments for six samples along rolling direction were carried out, respectively. And Fig. 7 shows the load–displacement curves of E-SPR joints obtained under different discharge energies. It could be seen that the maximum load of each curve exceeded 3 kN except the specimen with discharge energy of 4.9 kJ. With the different degree of CFRP sheets destruction between 4.9 kJ and 5.9 kJ, it could be demonstrated that the interlocking structure was one of the most influential factors on mechanical properties. Fig. 8 shows the bar chart of the maximum shear load with different discharge energies. It could be found that the specimen with discharge energy of 5.5 kJ had the highest maximum load compared with the others specimens, illustrating that the E-SPR joints obtained the best mechanical properties at the discharge energy of 5.5 kJ. When discharge energy increased from 4.9 kJ to 5.5 kJ, the interlocking structure enhanced due to the rivet pressing and the leg flaring. The serious destruction of CFRP made SPR joints easier

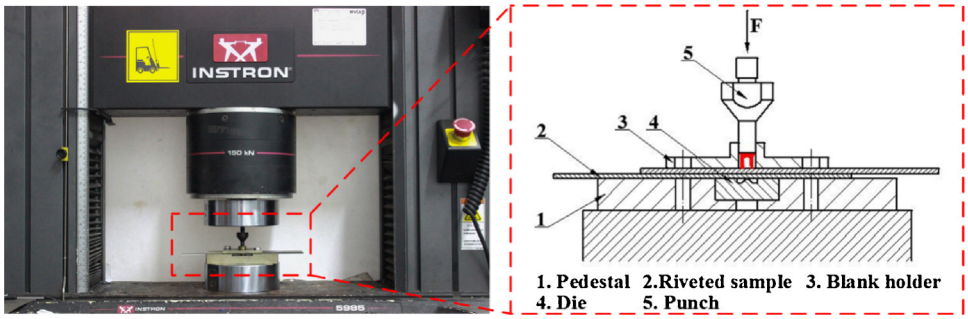

Fig. 5 – The P-SPR process experiments and diagram using 5985 universal testing machine.

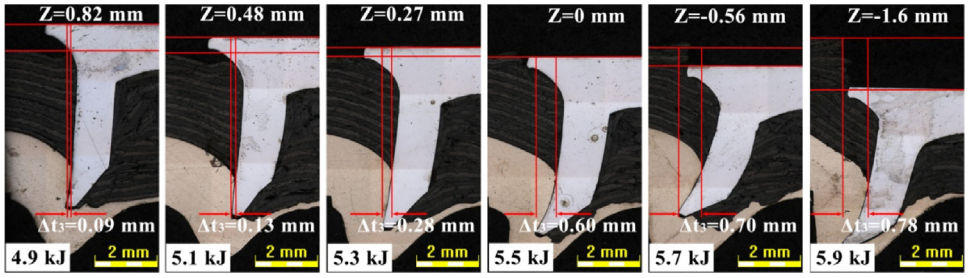

Fig. 6 – The cross-section geometries of the E-SPR joints with different discharge energies.

failure with the continue increasing of discharge energies. Therefore, the discharge energy of 5.5 kJ was the optimal process parameter.

3.2. *Dimension analysis*

In order to compare the structural parameters between the E-SPR and P-SPR joints, their typical cross-section (as shown in Fig. 9) was observed. Actually, the head height (Z) is considered to be the only evaluation index in the appearance of joints when there is no defect, such as fracture. It could be seen that the head height (Z) of the E-SPR (0.27 mm) was close to that of P-SPR (0.23 mm) joints. This demonstrated that the two kind joints were comparable. The rivet legs symmetry showed that the joints had a good formability. All joints formed interlocking structures. The rivet legs were in a large expansion, and did not generate excessive bending and yield phenomenon. It could be seen that both SPR joints had no obvious excessive stratification damage in the upper surface of CFRP sheets. The bottom part of Al sheets did not rupture, and the material flow retained a certain margin. The remaining thickness of the rivet leg was sufficient and no cracks were observed in the rivets. These results showed that both processes could provide a better SPR joint with certain mechanical strength.

Four samples for each riveting process were measured in order to compare the two processes. Amount change rates (n) were the ratio of the difference between E-SPR and P-SPR parameters values to P-SPR parameters values. The detailed comparing results about the maximum diameter, bottom thickness, remaining thickness, undercut amounts and amount change rates were shown in Table 4.

It could be found that the average bottom thickness Δt_1 and the remaining thickness Δt_2 of the E-SPR joints were 17.4% lower and 16.7% higher than that of P-SPR joints, respectively. The average undercut Δt_3 of E-SPR joints was 142.9% higher than that of P-SPR joints. The larger undercut of E-SPR joints contributed to the joint interlock performance. It could be found that undercut could substantial increase when using high loading velocity and high load of SPR joints. Compared with the undercut, bottom thickness and remaining thickness of E-SPR joints with high loading velocity were closer to that of P-SPR and indicated that the loading velocity had little influence on it. The E-SPR and P-SPR joints had a certain allowance of remaining thickness, and ensured a high quality of joints which were difficult to fracture. In addition, it could be found that two kind joints had enough distance between the rivet leg and joint bottom. This could ensure the joints had very higher joining strength.

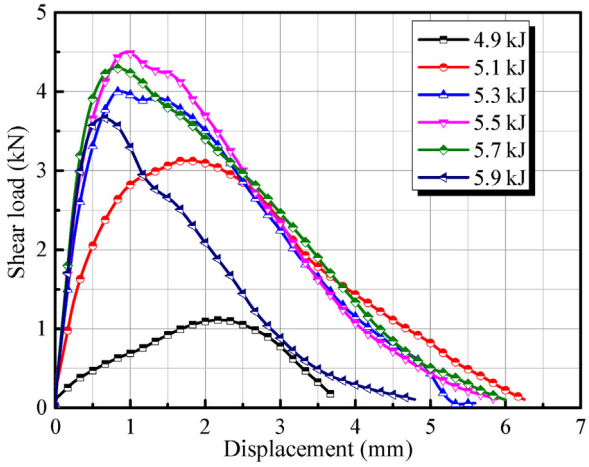

Fig. 7 – The shear load–displacement curves of E-SPR joints obtained under different discharge energies.

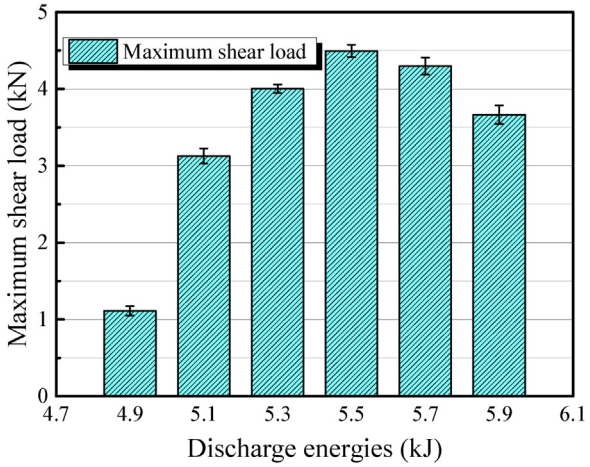

Fig. 8 – The maximum shear load–discharge energies bar chart of E-SPR joints.

3.3. *Microtopography comparison between E-SPR and P-SPR*

3.3.1. *Cross-section observations of joints*

Fig. 10 shows microtopography observations on the cross-section areas of riveted joints with the same joints as shown in Fig. 9. It could be seen that CFRP materials in both joints were fractured. As for E-SPR joints, the CFRP ruptured at the center (zone 2) of the rivet. But for the P-SPR joints, the breakage occurred around the rivet legs (zone 1). The CFRP sheet of P-SPR joints generated breakage at the region around the inner wall of the rivet leg (zone 1) and tip (zone 3), while the area of E-SPR joints had less damage. At the region (zone 2) inside the rivet, CFRP materials of E-SPR joints were very symmetrical and the extrusion fracture occurred under the high-speed

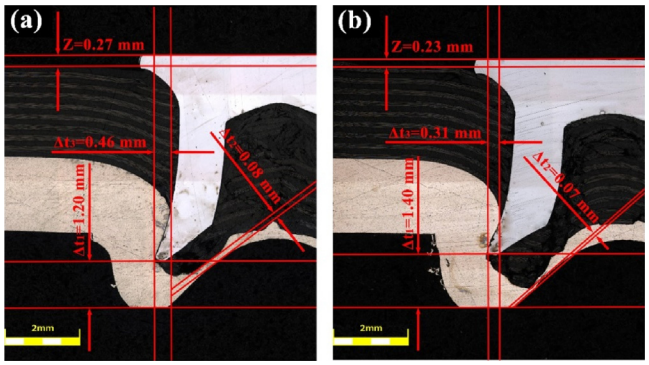

Fig. 9 – Schematic diagram of cross-section: (a) the E-SPR joint and (b) the P-SPR joint.

Table 4 – The P-SPR and E-SPR joints cross-section parameters (mm).

	Δt_1		Δt_2		Δt_3	
	E-SPR	P-SPR	E-SPR	P-SPR	E-SPR	P-SPR
Sample 1	1.35	1.56	0.18	0.09	0.35	0.27
Sample 2	1.35	1.57	0.08	0.17	0.43	0.20
Sample 3	1.52	1.99	0.19	0.13	0.60	0.11
Sample 4	1.30	1.56	0.12	0.10	0.64	0.27
Average	1.38	1.67	0.14	0.12	0.51	0.21
n	−17.4%		16.7%		142.9%	

impact. On the contrary, there was no fracture but had a large bending deformation for P-SPR joints. In addition, CFRP materials of P-SPR joints in the zone 3 had seriously broken into fiber fragments, rather than the fiber bundle was still intact of E-SPR joints. It could be found that the rivet of P-SPR joints was easier to loosen due to more fractured CFRP near the rivet leg. The abundant fragmented CFRP packed on the rivet periphery, which hindered the rivet leg from the expansion during the P-SPR process. However, it was more beneficial to expand the rivet legs during the E-SPR process due to the stratification of CFRP. This caused a higher undercut for E-SPR joints than that of P-SPR joints. It could be found that high impact speed made the CFRP sheet fracture in centrality of the rivet. Thus, the fractured CFRP materials were in the strip form inside the rivet of E-SPR joints. In P-SPR joints, parts of CFRP materials on the rivet leg were pressed into the bottom, which caused the partial the region was triangular in the zone 3.

3.3.2. *Micro hardness distribution*

Compared with the interlocking structure of E-SPR and P-SPR joints, the hardness of the rivet is also an important factor to influencing the joint forming. In order to further assess the quality of riveted joints, the hardness values of rivets were measured for E-SPR and P-SPR joints, respectively. The semi-tubular self-piercing rivet was a centrally symmetrical structure. Consequently, half of the rivet cross-section was selected for hardness measurements. As shown in Fig. 10, it could be also found that there were no greater plastic deformations on the rivet head during the joint forming process compared with the expended and bent rivet leg. Therefore, the rivet could be divided into two parts through the different degree of deformation: rivet head and rivet leg.

Fig. 11(a) presents that hardness values on the route 1 of rivet head had little data fluctuation, and the average hardness value was about 750 HV for both E-SPR and P-SPR joints. Comparing with the original hardness, it could be found that the hardness values were almost unchanged on route 1. This indicated that there was no deformation strengthening in rivet head. In addition, results also showed the hardness in rivet head had little difference between E-SPR and P-SPR joints. However, the average hardness value of E-SPR joints (830.92 HV) was 7.05% higher than that of P-SPR joints (776.18 HV) in the route 2 (rivet radial) of the rivet leg. This implied that the rivet of E-SPR joints had better work hardening effect. In addition, it could be found that both E-SPR and P-SPR joints had small plastic deformations in the route 2 of the rivet leg, while the plastic deformation of the

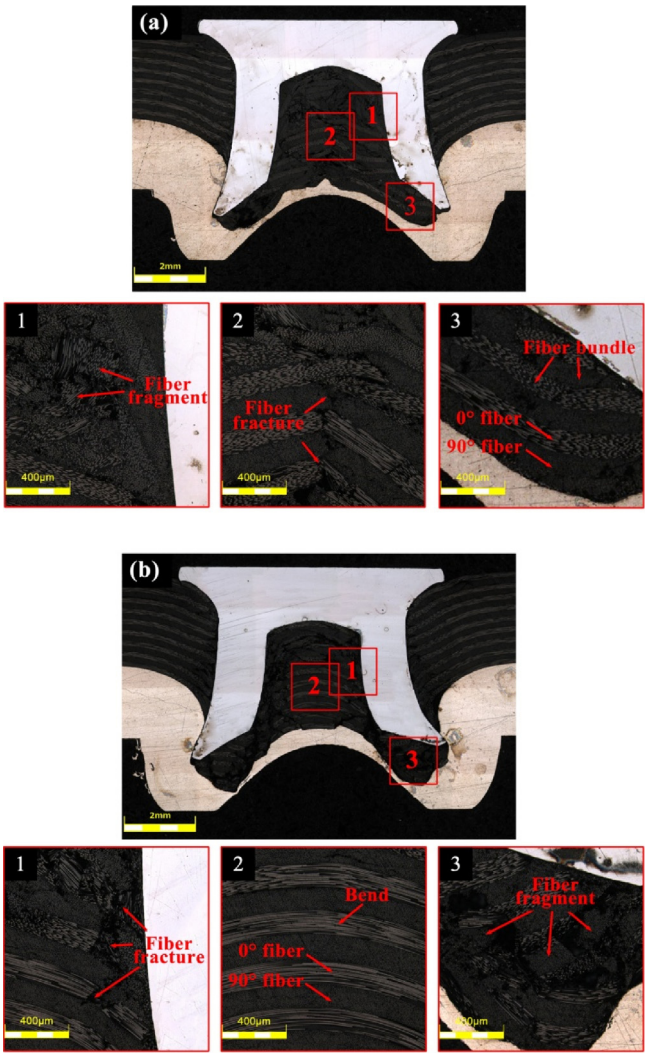

Fig. 10 – Microtopography observations in the cross-section areas of riveted joints and typical areas: (a) the E-SPR joint and (b) the P-SPR joint.

rivet mainly occurred in route 3 (rivet axial) of the rivet leg. It could be seen that the larger deformations were in positions closer to the tip of rivet. For P-SPR joints, hardness values increased slowly from the point 1 to the point 7. This showed that the rivet had a work hardening effect under cold plastic deformation. The rivet hardness values of E-SPR joints had the peak value in the center of the leg, which indicated that both sides of rivet legs were inward extruded and caused the center of legs could be significantly enhanced during the high-speed riveting. The average hardness value (823.4 HV) of route 3 of E-SPR joints was 7.78% higher than that (764.0 HV) of P-SPR joints. This demonstrated that the E-SPR process (under high-speed loading) had more obvious strengthening effect to rivet comparing with P-SPR process.

In a word, the optimum discharge energy of E-SPR process was obtained through microtopography analysis. It explained that the undercut value of E-SPR joints was higher than that of P-SPR joints around 150%. At the same time, the analysis of micro-hardness illustrated that higher strength of rivet ensured better strength of E-SPR joints.

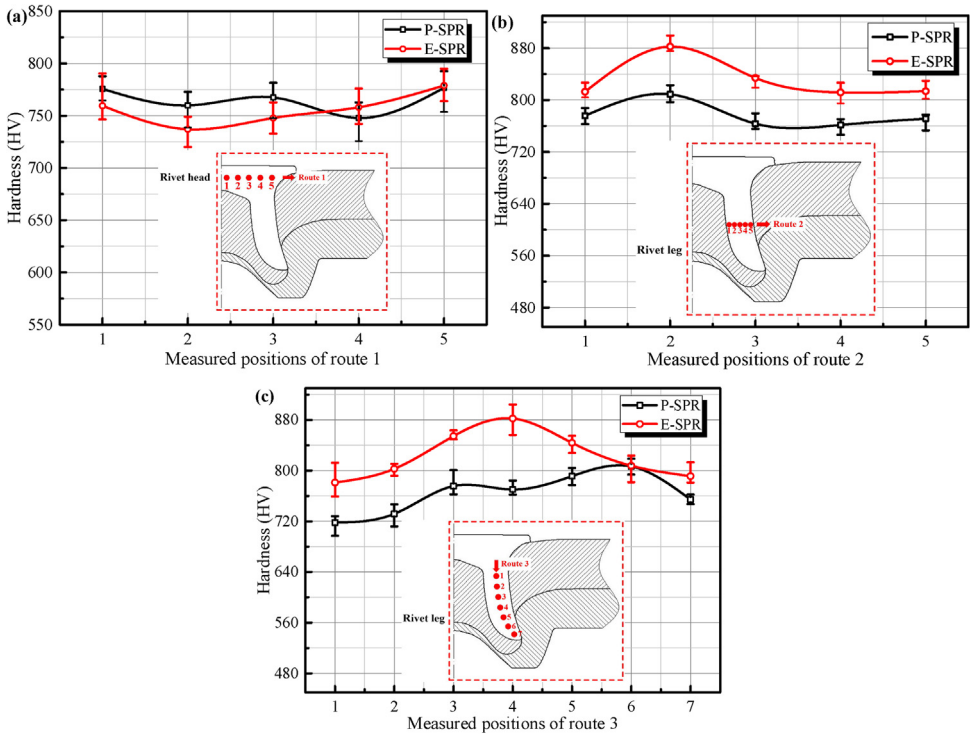

Fig. 11 – Rivet hardness comparison in different routes: (a) the route 1, (b) the route 2 and (c) the route 3.

3.4. *Mechanical properties comparison between E-SPR and P-SPR*

3.4.1. *Shear test*

Four repeated experiments were out performed for E-SPR and P-SPR specimens, respectively. Fig. 12 shows the typical shear load-displacement curves and loading rate-displacement curves. The detailed experiment results were in Table 5. The loading rate (α) was the differential of the shear load to the displacement. It could be seen from Fig. 11 that the shear load-displacement trend of E-SPR joints and P-SPR joints was approximately same. The maximum shear load of E-SPR joints was higher than that of P-SPR joints. During the tensile-shear of riveted joints, the shear load-displacement curves could be divided into three stages according to the loading rate: the elastic stage (A), the yield stage (B) and the failure stage (C). In the elastic stage ($\alpha > 2$), α descended rapidly after reaching 15 kN/mm. The shear load of the SPR joint was almost linearly related to the tensile displacement. It could be seen that α value of the E-SPR joint was slightly higher than that of P-SPR joint. Therefore, the bearing load (3.01 kN) of E-SPR joints was 23.9% higher than that (2.43 kN) of P-SPR joints at the end of the elastic stage. Through the study of SPR joints cross-section, it could be found that the elastic deformation of tension was mainly affected by the rivet and the bottom aluminum sheet. Also, the rivet of E-SPR joints had higher hardness value and was more difficult to yield and generate plastic deformation. In contrast, the structural deformation could occur easily of P-SPR joints due to the lower rivet strength and interlocking effect.

In the yield stage ($0 < \alpha < 2$), the contact area between the Al sheet and the CFRP sheet decreased that the shear loads were mainly provided by interlock force of joints. The plastic deformations caused the stiffness reduction of SPR joints. As the loading rates varied gently, the shear loads increased slowly. The loading rate of the E-SPR and the P-SPR were almost same at the yield stage, which indicated that the shear loads were only related to strengths of Al sheet, CFRP sheet and rivet at this stage. The average peak shear load (4.33 kN) of E-SPR joints was 16.4% higher than that (3.72 kN) of P-SPR joints. It could be found that the elastic stage had a decisive effect on the maximum shear loads of joints.

At the failure stage ($\alpha < 0$), shear loads gradually decreased and rivets started to fall off. It could be found that the residual resistance decreased linearly after the failure of the interlocking structure of joints. It could be seen that the loading rate of

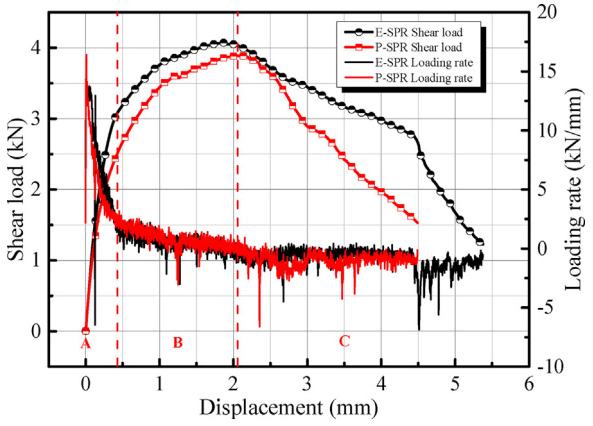

Fig. 12 – The shear load and loading rate–displacement curves of E-SPR and P-SPR specimens.

Table 5 – Maximum shear loads (MSL) for E-SPR and P-SPR tests (kN).

Samples	MSL for E-SPR tests	MSL for R-SPR tests
1	3.98	3.09
2	4.93	3.80
3	4.07	3.89
4	4.33	4.11
Average	4.33	3.72

E-SPR joints was higher than that of P-SPR joints, which illustrated that the E-SPR joints had better resistance to deformations and better energy absorption. In general, it could be found that E-SPR joints had better shear bearing performance than that of P-SPR joints.

3.4.2. *Shear failure process analysis*

Fig. 13(a) and (b) show fracture appearances of E-SPR and P-SPR joints, respectively. It could be seen that the both joints were ruptured by shear load. This was typical and not an accidental failure mode. In addition, it could be also observed that fracture appearances of two joints still had some differences. The rivet of E-SPR joints stayed in the Al sheet, while rivet of P-SPR joints stayed in the CFRP sheet. This illustrated that the rivet of E-SPR joints was more tightly locked in the Al sheet than P-SPR joints. The results were consistent with the above microtopography analysis. In addition, the CFRP damage mainly concentrated on the verge of hole and the damage degree for the E-SPR joints was more serious than that of P-SPR joints. CFRP failure modes of both joints were layer separation and fiber bundle fracture, as shown in zone 1. It could be seen that the fiber of E-SPR joints fractured smoothly, rather that the fiber fracture in radial direction of P-SPR joints. Low puncture speed led to CFRP around the rivet was more prone to radial fracture during the P-SPR. As zone 2, the extrusion of rivet caused CFRP materials of E-SPR joints had more fiber fracture along shear load direction, rather than the resin peeling fiber fragments of P-SPR joints. It could be found that large fiction led to the resin failure of carbon fibers during the P-SPR. The zone 3 showed that the fiber broken and layer separation occurred along the vertical shear direction of E-SPR and P-SPR joints. However, the fiber bundle fracture of E-SPR was smoother than that of P-SPR, as shown in zone 4. It could be found that P-SPR joints were more prone to shear failure due to the existence of CFRP fragments around the rivet.

According to the above analysis, the shear failure mechanisms were concluded. Fig. 14 shows the shear failure processes of the E-SPR and P-SPR joints in different tensile displacement. It could be found that the CFRP fractured firstly around rivet of the E-SPR joint. On the contrary, the interlocking structure of P-SPR joint failed which was the reason why the rivet finally stayed in CFRP sheet. It could be found that rivets of E-SPR and P-SPR joints firstly inclined under the shear load. With the increase of displacement, the asymmetry force made the bending angle increase gradually. The bending began with the shorter end of joints. The friction between the sheets decreased rapidly because the contact area between sheets decreased. When the contact area between the rivet and CFRP sheet reached a certain value, the interlocking structure between the rivet and the bottom sheet started to be

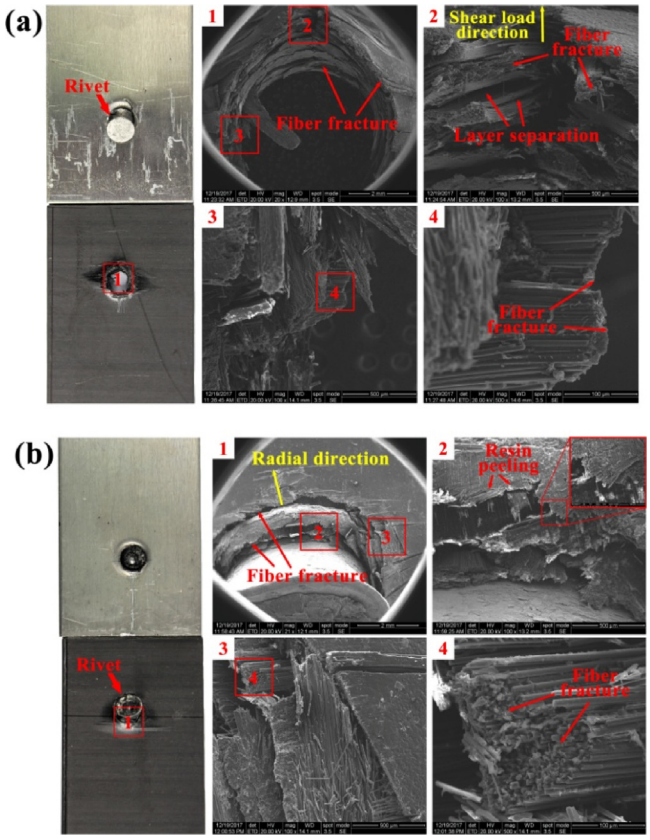

Fig. 13 – The shear failure appearance of lap joints: (a) the E-SPR joint and (b) the P-SPR joint.

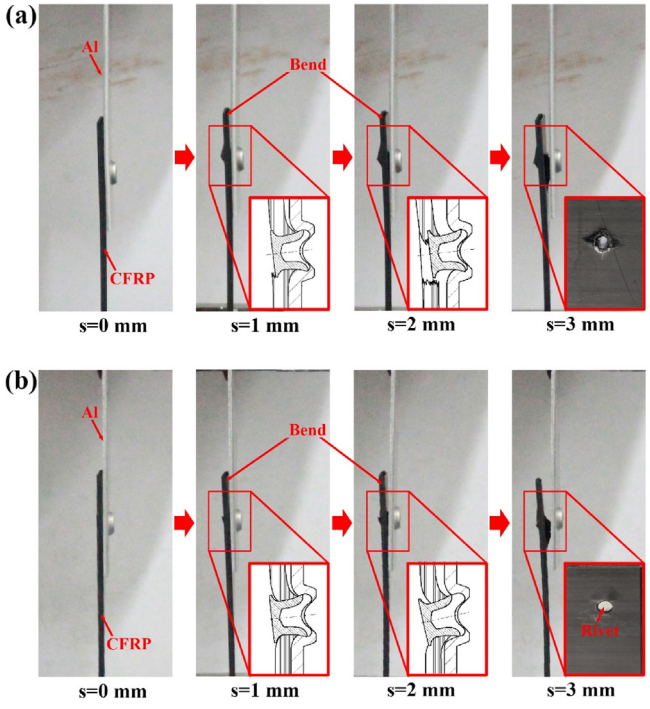

Fig. 14 – Shear failure processes: (a) the E-SPR joint and (b) the P-SPR joint.

Table 6 – Comprehensive comparison between the E-SPR and P-SPR.

Aspects	E-SPR	P-SPR	Comparing results
Joining time per riveting	1 ms	3 min	Significantly reduced
Joining quality	MSL of 4.33 kN	MSL of 3.72 kN	Increased by 16.4%
Capital cost	Electromagnetic forming system	Hydraulic system	Costs flat
Maintenance	Discharging coil	Hydraulic oil	Convenient maintenance

destroyed. At moment, the shear load was mainly carried by the CFRP sheet and interlocking structure between the rivet and the Al sheet. As shown in Fig. 14(a), it could be found that CFRP sheets of E-SPR joints were completely failure due to the large undercut and high interlock strength. The shear strength of E-SPR joints was equaled to the CFRP strength around the rivet. For the interlocking structure failure of P-SPR joints, it could be observed from Fig. 14(b) that the rivet pulled out and stayed in the CFRP sheet due to the inadequate undercut value. The shear strength of P-SPR joints was equaled to the interlocking structure strength and lower than the CFRP strength around the rivet. It could be found from the microtopography analysis that the CFRP strength around the rivet of E-SPR joints was higher than that of P-SPR joints.

To sum up, the E-SPR and P-SPR samples had significant different in joining time, joining quality and maintenance, as shown in Table 6. The E-SPR process with a higher riveting speed had shorter time-consuming, which could greatly improve the efficiency in practical applications. The E-SRP samples had better tensile-shear strength than that of P-SPR. Though the capital cost of E-SPR and P-SPR system were almost equal, the maintenance of discharging coil was more convenient and environmentally friendly.

4. Conclusions

In order to study joining performance of E-SPR and P-SPR joints, microtopography observations, hardness tests and tensile-shear tests were carried out. The major conclusions are drawn as follows:

1. The microtopography analysis showed that the CFRP damage extent degree and rivet leg expansion affected the strength of E-SPR joints. Considering results of the microtopography appearance and tensile-shear strength, the optimal process parameter for E-SPR technique was the discharge energy of 5.5 kJ.
2. The undercut value of E-SPR joints was around 150% higher than that of P-SPR joints. While the bottom thickness and remaining thickness of E-SPR and P-SPR joints only had a difference around 15%.
3. The larger deformation caused that hardness values of the rivet leg were higher than that of the rivet head. In addition, the hardness values of E-SPR joints on the rivet leg were higher than that of P-SPR joints. This illustrated that the high strain rate during the E-SPR process had higher strengthening effect on rivet leg comparing with P-SPR.
4. The better interlocking structure caused that the E-SPR joints exhibited higher maximum shear strength than that of P-SPR joints. Due to the higher undercut, the shear fracture appearances showed that the rivet of E-SPR joints stayed in the Al sheet. But rivet of P-SPR joints stayed in the CFRP sheet.

Data availability

The raw/processed data required to reproduce these findings cannot be shared at this time due to technical or time limitations.

Ethical statement

Authors state that the research was conducted according to ethical standards.

Acknowledgements

This work was supported by the Foundation for Innovative Research Groups of the National Natural Science Foundation of China (No. 51621004) and the National Key Research and Development Program of Hunan Province (2017GK2090).

REFERENCES

[1] H. Rao, J. Kang, G. Huff, K. Avery, Impact of specimen configuration on fatigue properties of self-piercing riveted aluminum to carbon fiber reinforced polymer composite, Int. J. Fatigue 113 (2018) 11–22.
[2] F. Hirsch, S. Müller, M. Machens, R. Staschko, N. Fuchs, M. Kästner, Simulation of self-piercing riveting processes in fibre reinforced polymers: material modelling and parameter identification, J. Mater. Process. Technol. 241 (2017) 164–177.
[3] E. Eusebi, Composite intensive vehicles: past, present and future, in: Structure Materials Challenges Next Generation Vehicle, US Department Commercial, Washington, DC, 1995.
[4] N.A. Gjostein, Technology Needs Beyond PNGV, Basic Needs Vehicle Future New Orleans, Louisiana (5 January 1995), 1995.
[5] X. He, I. Pearson, K. Young, Self-pierce riveting for sheet materials: state of the art, J. Mater. Process. Technol. 199 (2008) 27–36.
[6] L. Huang, J. Moraes, D. Sediako, J. Jordan, H. Guo, X. Su, Finite-element and residual stress analysis of self-pierce riveting in dissimilar metal sheets, J. Manuf. Sci. Eng. 139 (2017), 021007-1–021007-11.
[7] A. Pramanik, A. Basak, Y. Dong, P. Sarker, M. Uddin, G. Littlefair, A. Dixit, S. Chattopadhyaya, Joining of carbon fibre

reinforced polymer (CFRP) composites and aluminium alloys – a review, Composite A 101 (2017) 1–29.
[8] M. Fu, P. Mallick, Fatigue of self-piercing riveted joints in aluminum alloy 6111, Int. J. Fatigue 25 (2003) 183–189.
[9] Y. Miyashita, Y. Teow, T. Karasawa, N. Aoyagi, Y. Otsuka, Y. Mutoh, Strength of adhesive aided SPR joint for AM50 magnesium alloy sheets, Proc. Eng. 10 (2011) 2532–2540.
[10] Y. Abe, T. Kato, K. Mori, Self-piercing riveting of high tensile strength steel and aluminium alloy sheets using conventional rivet and die, J. Mater. Process. Technol. 209 (2009) 3914–3920.
[11] D. Li, A. Chrysanthou, I. Patel, G. Williams, Self-piercing riveting – a review, Int. J. Adv. Manuf. Technol. 92 (2017) 1777–1780.
[12] J. Kang, H. Rao, R. Zhang, K. Avery, X. Su, Tensile and fatigue behavior of self-piercing rivets of CFRP to aluminium for automotive application, IOP Conf. Ser. Mater. Sci. Eng. 137 (2016) 12–25.
[13] X. He, Y. Wang, Y. Lu, K. Zeng, F. Gu, A. Ball, Self-piercing riveting of similar and dissimilar titanium sheet materials, Int. J. Adv. Manuf. Technol. 80 (2015) 2105–2110.
[14] Z. Xie, W. Yan, C. Yu, T. Mu, L. Song, Tensile capacity of self-piercing rivet connections in thin-walled steel structures, J. Construct. Steel Res. 144 (2018) 211–220.
[15] R. Cacko, Review of different material separation criteria in numerical modeling of the self-piercing riveting process-SPR, Arch. Civil Mech. Eng. 8 (2008) 21–30.
[16] W. Presz, R. Cacko, Analysis of the influence of a rivet yield stress distribution on the micro-SPR joint-initial approach, Arch. Civil Mech. Eng. 10 (2010) 69–75.
[17] W. Yan, Z. Xie, C. Yu, L. Song, H. He, Experimental investigation and design method for the shear strength of self-piercing rivet connections in thin-walled steel structures, J. Construct. Steel Res. 133 (2017) 231–240.
[18] G.D. Franco, L. Fratini, A. Pasta, Influence of the distance between rivets in self-piercing riveting bonded joints made of carbon fiber panels and AA2024 blanks, Mater. Des. 35 (2012) 342–349.
[19] J. Mucha, The numerical analysis of the effect of the joining process parameters on self-piercing riveting using the solid rivet, Arch. Civil Mech. Eng. 14 (2014) 444–454.
[20] C. Zhang, R. Gou, M. Yu, Y. Zhang, Y. Qiao, S. Fang, Mechanical and fatigue properties of self-piercing riveted joints in high-strength steel and aluminium alloy, J. Iron Steel Res. Int. 24 (2017) 214–221.
[21] X. He, L. Zhao, C. Deng, B. Xing, F. Gu, A. Ball, Self-piercing riveting of similar and dissimilar metal sheets of aluminum alloy and copper alloy, Mater. Des. 65 (2015) 923–933.
[22] R. Haque, Y. Durandet, Strength prediction of self-pierce riveted joint in cross-tension and lap-shear, Mater. Des. 108 (2016) 666–678.
[23] O. Hahn, R. Neugebauer, G. Leuschen, C. Kraus, R. Mauermann, Research in impulse joining of self pierce riveting, in: 3rd International Conference on High Speed Forming – 2008, Dortmund, Germany, 2008.
[24] B. Wang, C. Hao, J. Zhang, H. Zhang, A new self-piercing riveting process and strength evaluation, J. Manuf. Sci. Eng. 128 (2006) 580–587.
[25] D. Li, L. Han, A. Chrysanthou, M. Shergold, G. Williams, The effect of setting velocity on the static and fatigue strengths of self-piercing riveted joints for automotive applications, in: TMS Annual Conference, 2014.
[26] F. Li, J. Mo, J. Li, L. Huang, H. Zhou, Formability of Ti–6Al–4V titanium alloy sheet in magnetic pulse bulging, Mater. Des. 52 (2013) 337–344.
[27] X. Cui, J. Li, J. Mo, J. Fang, Y. Zhu, K. Zhong, Investigation of large sheet deformation process in electromagnetic incremental forming, Mater. Des. 76 (2015) 86–96.
[28] X. Zhang, H. Yu, C. Li, Microstructure investigation and mechanical property analysis in electromagnetic riveting, Int. J. Adv. Manuf. Technol. 78 (2015) 613–623.
[29] V. Psyk, D. Risch, B.L. Kinsey, A.E. Tekkaya, M. Kleiner, Electromagnetic forming – a review, J. Mater. Process. Technol. 211 (2011) 787–829.
[30] E.A. Repetto, R. Radovitzky, M. Ortiz, R.C. Lundquist, D.R. Sandstrom, A finite element study of electromagnetic riveting, J. Manuf. Sci. Eng. 121 (1999) 61–68.
[31] J. Cui, L. Qi, H. Jiang, G. Li, X. Zhang, Numerical and experimental investigations in electromagnetic riveting with different rivet dies, Int. J. Mater. Form. (2017) 1–15.
[32] B.W. Huffer, HH54 rugged and reliable handheld EMR, in: Aerospace Technology Conference and Exposition, 2009.
[33] L. Zhao, X. He, B. Xing, Y. Lu, F. Gu, A. Ball, Influence of sheet thickness on fatigue behavior and fretting of self-piercing riveted joints in aluminum alloy 5052, Mater. Des. 87 (2015) 1010–1017.
[34] H. Jiang, G. Li, X. Zhang, J. Cui, Fatigue and failure mechanism in carbon fiber reinforced plastics/aluminum alloy single lap joint produced by electromagnetic riveting technique, Compos. Sci. Technol. 152 (2017) 1–10.
[35] R. Haque, Quality of self-piercing riveting (SPR) joints from cross-sectional perspective: a review, Arch. Civil Mech. Eng. 18 (2018) 83–93.
[36] H. Jiang, T. Luo, G. Li, X. Zhang, J. Cui, Fatigue life assessment of electromagnetic riveted carbon fiber reinforce plastic/aluminum alloy lap joints using Weibull distribution, Int. J. Fatigue 105 (2017) 180–189.